

# Optimum design of a double-sided permanent magnet linear synchronous motor to minimize the detent force

## Authors

Mehrdad Makki <sup>a\*</sup>  
Siroos Hemmati <sup>a</sup>

<sup>a</sup> Department of Electrical Engineering, Kermanshah University of Technology, Kermanshah, Iran

## ABSTRACT

*In the permanent magnet linear synchronous motor (PMLSM), force ripple is harmful, useless and disturbing. The force ripple is basically composed of two components: detent force and mutual force ripple. This force is influenced by the geometric parameters of the permanent magnet (PM) motors; such as width, thickness and length of the magnet poles, length and thickness of the rotor and stator, and stator slot shape. For design optimization, the force ripple can be considered as the objective function and geometric parameters can be considered as design variables. In this paper, the distribution of magnetic flux density in the air gap is calculated using an analytical method, then detent force is computed by integrating the Maxwell stress tensor; that is expressed in terms of flux density distribution on the slot face and end face of the iron core of moving parts. The analytical result is compared with FEM simulation to verify the model. The geometric parameter effect on the detent force is investigated. Finally, using genetic algorithm, the optimum design of a linear synchronous motor with minimum detent force is obtained.*

## Article history:

Received : 9 August 2016  
Accepted : 21 January 2017

**Keywords:** Linear Brushless Permanent Magnet Motor, Detent Force, FEM, Analytical Methods, Genetic Algorithm.

## 1. Introduction

Linear brushless motors (LBMs) have a good capacity for speed control. Among LBMs, synchronous motors have a special place because they have advantages such as fewer space harmonics, grater energy efficiency, and are easier to control [1]. LBMs can be classified in two groups according to the stator type; slotted iron core and air core (slotless stator). The first type of motor is used in both the surface permanent magnet (SPM) and interior permanent magnet (IPM) motors [2]. The motor can be constructed in

single-sided or double-sided structures. The double-sided structure is appropriate for high-force density applications as it can produce much larger force in a given volume [2]. However, its large detent force, due to the end effects and cogging forces, is a significant drawback in high-precision motion control at low speed. Force ripple in a permanent magnet linear synchronous motor (PMLSM) with salient pole is a destructive factor. Basically, force ripple is composed of two components; detent force and mutual force ripple. In PM motors, detent force is created by interaction of the rotor magnetic field with the stator magnetic reluctance, while mutual force ripple is generated by the interaction of excitation current MMF with magnetic field or rotor magnetic reluctance

\*Corresponding author: Mehrdad Makki  
Address: School of Mechanical Engineering, College of Engineering, Kermanshah University of Technology, Iran  
E-mail address: m-maki@kut.ac.ir

[3,4]. In linear PM motor, the detent force has two components; the first component is due to the teeth ripple, which also exists in rotary motor known as the cogging force, and the other is end effect component, which exists only in linear motor because of finite length of the rotor.

Optimization methods have been studied in many papers. The ripple caused by tooth (i.e. cogging force) in linear motor, can be reduced with skewed PM [5,6], semi-closed slots [6,7], stator with auxiliary teeth [7,8], optimizing the shifted length of magnet pole and the ratio of magnet width to pole pitch [9] and asymmetric PM placement [10,11].

The end effect can be reduced by optimizing the rotor length [12, 13]. The mutual force ripple can be reduced by matching current waveform with the magnetic field distribution [14]. The flux density distribution can be expressed in terms of geometric parameters. So, for design optimization, the force ripple can be considered as the objective function and geometric parameters as design variables. This study presents optimization of the motor using genetic algorithm to achieve minimum detent force and verifies the results by FEM simulation. The detent force is computed by integrating the Maxwell stress tensor, expressed in terms of flux density distribution

on the slot face and end face of the iron core of moving parts [15]. In this paper, the influence of geometric parameters (such as width, thickness and shape of the PM etc.) on the detent force in a double-sided PMLSM is analyzed using FEM. Also, the genetic algorithm is linked to the FEM software so that the obtained results from the algorithm can be evaluated by the finite element method in each step of simulation.

## 2. Geometric structure and analytical model

Figure 1 shows a double-sided permanent magnet motor. Generally, these motors have two types of structures; primary mover (armature mover) and secondary mover (rotor mover). Commonly, the mover part is shorter than the fixed part. Each of these motors are divided into two categories depending on the type of motor structure; 1- two external armature system and one internal excitation system (Fig. 1.a) and 2- one internal armature system and two external excitation system (Fig. 1.b).

PM poles are mounted on the rotor and the rotor is moving. The parameters of double-sided permanent magnet linear motor under study are listed in Table 1. Among these parameters, the geometric parameters such as

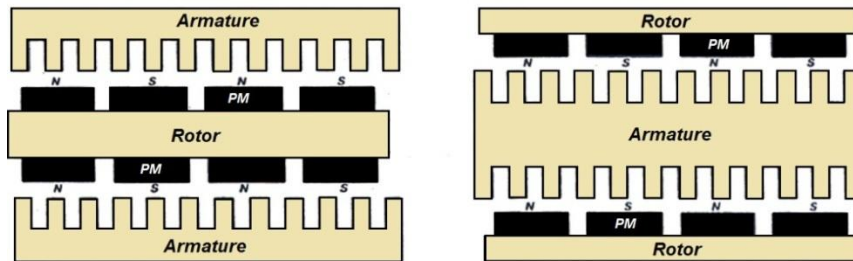


**Fig.1.** Double-sided PM LSMs with: (a) two external armature system and one internal excitation system, (b) one internal armature system and two external excitation system

**Table 1.** List of parameters for double-sided PMLSM-rotor moving-two external armature system and one internal excitation system

Parameters	Symbols	Value
Slot pitch	$\tau_s$	13.5mm
Slot width	$\omega_s$	8mm
Armature thickness	$h_A$	48mm
Rotor thickness	$h_R$	36mm
Rotor length	$l_r$	165.6mm
Pole pitch	$\tau$	82.8mm
Magnet thickness	$h_m$	7.5mm
Magnet width	$\omega_m$	50.4mm
Air gap	$g$	1mm

width of magnet ( $\omega_m$ ), thickness of magnet ( $h_m$ ), length of rotor ( $l_r$ ), thickness of rotor ( $h_r$ ) and slot pitch ( $\tau_s$ ) are considered as design variables.

The two-dimensional electromagnetic field distribution will be determined based on the following assumptions;

- a) The armature core is an isotropic and slotless cube with a magnetic permeability tending to infinity and an electric conductivity tending to zero.
- b) PMs are isotropic, magnetized in the normal direction (y coordinate) and have zero electric conductivity.
- c) Each PM is represented by an equivalent coil embracing the PM and carrying a fictitious surface current which produces an equivalent magnetic flux.
- d) The magnetic permeability of the space between PMs is equal to that of PMs.
- e) The yoke of the rotor is an isotropic cube with magnetic permeability tending to infinity and electric conductivity tending to zero.

The equations are obtained for only one side of the motor. Figure 2 shows one side of the motor with its parameters. Figure 3 shows a simplified model for the analysis of the magnet and air gap field [16].

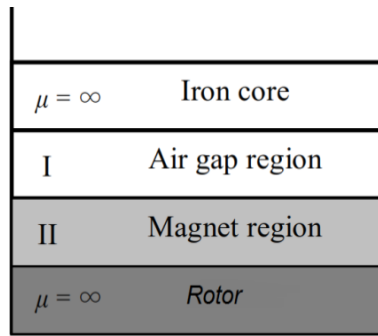


Fig.3. simplified model for the analysis

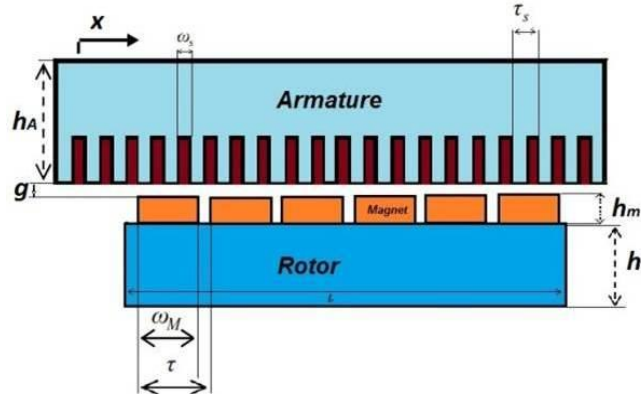


Fig.2. One side of the motor with its parameters

### 2.1. Calculation of the detent force

The following analytical method is used to calculate the detent force. The simplified in terms of magnetic vector potential ( $A$ ). In the air gap region, the Laplace equation is given by

$$\frac{\partial^2 A_I}{\partial x^2} + \frac{\partial^2 A_I}{\partial y^2} = 0. \quad (1)$$

In the magnet region, the Poisson equation is given as

$$\frac{\partial^2 A_{II}}{\partial x^2} + \frac{\partial^2 A_{II}}{\partial y^2} = \mu_M J_M. \quad (2)$$

where  $A_I$  and  $A_{II}$  are the magnetic vector potential of each region,  $\mu_M$  is the permeability of the magnet and  $J_M$  is the distribution of current density in the current sheet model, which generates a magnetic field equal to the field of magnets [17]. The current density can be expressed as a function of magnet geometry and properties, as follows:

$$J_M(x) = \frac{B_r}{\mu_M} \sum_{n=1,3,5,\dots}^{\infty} \frac{4}{\tau} \sin\left(\frac{\alpha n \pi}{2}\right) \sin\left(\frac{n \pi x}{\tau}\right), \quad (3)$$

where  $B_r$  is the permanent magnetic flux density,  $\tau$  is the pole pitch and  $\alpha$  is the ratio of width of the magnet to the pole pitch. The corresponding general solution of Eq. (1) and (2) are [18]

$$A_I(x) = \sum (C_1 e^{\frac{n \pi y}{\tau}} + C_2 e^{-\frac{n \pi y}{\tau}}) \sin\left(\frac{n \pi x}{\tau}\right) \quad (4)$$

$$A_{II}(x) = \sum (C_3 e^{\frac{n \pi y}{\tau}} + C_4 e^{-\frac{n \pi y}{\tau}} + \frac{4 B_r \tau}{n^2 \pi^2} \sin\left(\frac{\alpha n \pi}{2}\right) \sin\left(\frac{n \pi x}{\tau}\right)) \quad (5)$$

From the assumption that the permeability of the iron core and stator is infinite, the boundary conditions are given as

At:  $y=g \rightarrow H_{xI} = 0$ ,

At:  $y=0$  (at the intersection between the region II and rotor region)  $\rightarrow H_{xII} = H_{xI}$  and  $B_{yII} = B_{yI}$  and

At:  $y=h_M \rightarrow H_{xI} = 0$ .

From these boundary conditions, the constants of Eq. (4) and (5) can be determined from

$$C_1 = C_2 \times e^{\frac{2n\pi g}{\tau}}$$

$$C_3 = C_4 e^{\frac{2n\pi h_M}{\tau}}$$

$$C_2 =$$

$$\frac{4B_r \tau}{n^2 \pi^2} \times \sin\left(\frac{\alpha n \pi}{2}\right) \left/ \begin{array}{l} \left[ \left( e^{\frac{2n\pi g}{\tau}} + 1 \right) + \right. \\ \left. \frac{\mu_M \left( e^{\frac{2n\pi}{\tau}} + 1 \right) \left( e^{\frac{2n\pi h_M}{\tau}} + 1 \right)}{\mu_0 \left( e^{\frac{2n\pi h_M}{\tau}} - 1 \right)} \right] \end{array} \right.$$

$$C_4 = \frac{\mu_M \left( e^{\frac{2n\pi g}{\tau}} + 1 \right)}{\mu_0 \left( e^{\frac{2n\pi h_M}{\tau}} - 1 \right)}$$

where  $h_M$  is the thickness of PM and  $g$  is the air gap length, flux density distribution can be derived by curling the magnetic vector potential which is normal to the xy plane. The flux density distribution is then given by

$$\begin{aligned} B &= \nabla \times A \\ &= \left( \frac{\partial}{\partial x} \vec{i} + \frac{\partial}{\partial x} \vec{j} + \frac{\partial}{\partial x} \vec{k} \right) \times A \vec{k} \\ &= \frac{\partial A}{\partial x} \vec{i} + \frac{\partial A}{\partial x} \vec{j}. \end{aligned} \quad (6)$$

In Eq.(6), the flux density distribution on the iron core of the armature is interfaced with the air gap and since it has only one normal component, it is given by

$$\begin{aligned} B_y(x) &= \frac{\partial A_I}{\partial x} \\ &= \sum_{n=1,3,5,\dots}^{\infty} \frac{n\pi}{\tau} \left( C_1 e^{\frac{n\pi g}{\tau}} + C_2 e^{-\frac{n\pi g}{\tau}} \right) \\ &\quad \times \cos\left(\frac{n\pi x}{\tau}\right). \end{aligned} \quad (7)$$

The slot on the iron core of the armature changes the length of the air gap with the Carter's factor. So, the flux density distribution is modified for the slot effect; that is

$$\begin{aligned} B_{ys}(x) &= \alpha_s \sum_{n=1,3,5,\dots}^{\infty} \frac{n\pi}{\tau} \left( C_1 e^{\frac{n\pi y}{\tau}} + C_2 e^{-\frac{n\pi y}{\tau}} \right) \\ &\quad \times \cos\left(\frac{n\pi x}{\tau}\right), \end{aligned} \quad (8)$$

$$\alpha_s = \frac{\mu_M g + h_M}{\mu_M g + h_M + 0.5 \mu_M \pi r_s},$$

$$\text{for } (k-1)\tau_s - \frac{\omega_s}{2} \leq x \leq (k-1)\tau_s + \frac{\omega_s}{2}$$

$$K = 1, 2, 3, \dots, Q_s,$$

where  $\tau_s$  and  $\omega_s$  are the slot pitch and slot width, respectively;  $r_s$  is a function of  $x$  and  $Q_s$  is the number of armature slots that are underneath the rotor.

The detent force is calculated by integrating the Maxwell stress tensor along the slot face on the iron core of the armature [19]. According to this assumption, the flux density distribution has a single normal component at the surface of the iron core as shown in Fig. 4. From the flux density distribution, the normal and tangential forces acting on each surface of the armature are given by;

$$\begin{aligned} F_n &= \frac{L}{2\mu_0} \int [B_n^2 - B_t^2] dl \\ &= \frac{L}{2\mu_0} \int B_n^2 dl \end{aligned} \quad (9)$$

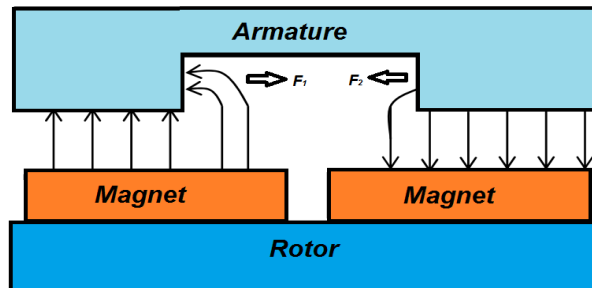


Fig.4. The flux density distribution at the surface of the iron core and its forces

$$F_t = \frac{L}{\mu_0} \int B_n B_t dl = 0 \quad (10)$$

where L is the effective length of the armature core and l is an integral path along the surface of iron core. The cogging force component (tooth ripple) is calculated by summation of the normal forces at each slot area (Eq. 11), where  $x_0$  is position of the magnet poles relative to the armature.

End effect component of the detent force is calculated by summation of the forces at each end area of the rotor as shown in Fig. 5. Thus,

$$x_{11} = x_0 - \frac{\omega_s}{2} - \frac{\tau_s}{2} - d_t + h_r$$

$$x_{12} = x_0 - \frac{\omega_s}{2} - \frac{\tau_s}{2} - d_t$$

$$x_{22} = x_0 + (Q_s + 1)\tau_s + \frac{\omega_s}{2} + \frac{\tau_s}{2} + d_t + h_r$$

$$x_{21} = x_0 + (Q_s + 1)\tau_s + \frac{\omega_s}{2} + \frac{\tau_s}{2} + d_t$$

This force is proportional to the thickness and length of iron core. Thus, one way of reducing this force is to change the length and thickness of the core.

$$F_{cogging}(x_0) = \sum_{k=1}^{Q_s} F_k(x_0) = \sum_{k=1}^{Q_s} (F_{1k}(x_0) - F_{2k}(x_0)) =$$

$$\frac{L}{4\mu_0} \sum_{k=1}^{Q_s} \left\{ \left[ \sum_{n=1,3,\dots}^{\infty} B_{sn}^2 (x_{12} - x_{11} + \frac{\tau}{2n\pi} (\sin(\frac{2n\pi x_{12}}{\tau}) - \sin(\frac{2n\pi x_{11}}{\tau}))) + \sum_{m=n+2}^{n=1,3} B_{sn} B_{sm} (\frac{\tau}{(n-m)\pi} (\sin(\frac{(n-m)\pi x_{12}}{\tau}) - \sin(\frac{(n-m)\pi x_{11}}{\tau}))) + \right. \right.$$

$$\left. (\frac{\tau}{(n-m)\pi} (\sin(\frac{(n+m)\pi x_{12}}{\tau}) - \sin(\frac{(n+m)\pi x_{11}}{\tau}))) + \right. \left. (\frac{\tau}{(n+m)\pi} (\sin(\frac{(n+m)\pi x_{12}}{\tau}) - \sin(\frac{(n+m)\pi x_{11}}{\tau}))) \right] - \left[ \sum_{n=1,3,5}^{\infty} B_{sn}^2 (x_{22} - x_{21} + \frac{\tau}{2n\pi} (\sin(\frac{2n\pi x_{22}}{\tau}) - \sin(\frac{2n\pi x_{21}}{\tau}))) + \right.$$

$$\left. \sum_{m=n+2}^{n=1,3,\dots} B_{sn} B_{sm} (\frac{\tau}{(n-m)\pi} (\sin(\frac{(n-m)\pi x_{22}}{\tau}) - \sin(\frac{(n-m)\pi x_{21}}{\tau}))) + (\frac{\tau}{(n+m)\pi} (\sin(\frac{(n+m)\pi x_{22}}{\tau}) - \sin(\frac{(n+m)\pi x_{21}}{\tau}))) \right] \right\}, \quad (11)$$

where;

$$B_{sn} = \frac{n\pi}{\tau} (C_1 e^{\frac{n\pi g}{\tau}} + C_2 e^{-\frac{n\pi g}{\tau}})$$

$$B_{sm} = \frac{n\pi}{\tau} (C_1 e^{\frac{m\pi g}{\tau}} + C_2 e^{-\frac{m\pi g}{\tau}})$$

$$x_{11} = x_0 + (k - 1)\tau_s - \frac{\omega_s}{\pi}$$

$$x_{12} = x_0 + (k - 1)\tau_s$$

$$x_{22} = x_0 + (k + 1)\tau_s - \frac{\omega_s}{\pi}$$

$$x_{21} = x_0 + (k + 1)\tau_s$$

The equation of the end effect force is similar to the Eq. (11), but positions are different; hence,

#### 4.FEM simulation

##### 4.1.Influence of parameters on the detent force

In this paper, we discussed a double-sided permanent magnet linear synchronous motor with two magnetic poles. This model is designed following the parameters listed in Table 1. Figure 6 shows 2-D FEM model of this motor. Figure 7 shows the flux density distribution without injection current into the armature coils. Figure 8 shows the flux lines in the motor. Use of semi-closed slots on the stator instead of open slots presents a way to improve and reduce the detent force in the PMLSM. Figure 9 shows both type of slots.

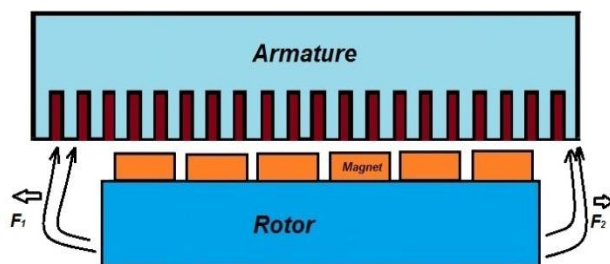


Fig.5. The flux density distribution at the end area of the rotor and its forces

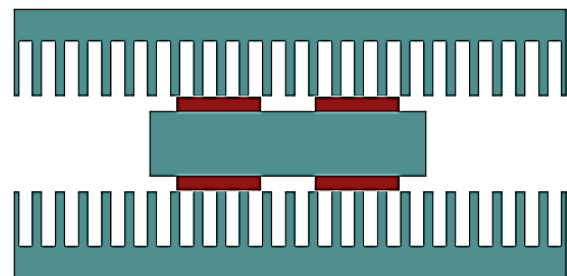


Fig.6. 2-D FEM model of the PMLSM

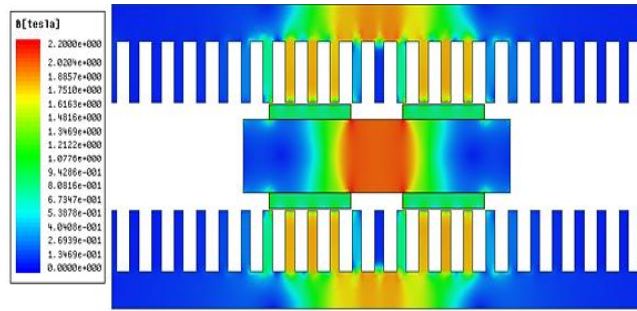


Fig.7. The flux density in system without injection current in to the armature coils

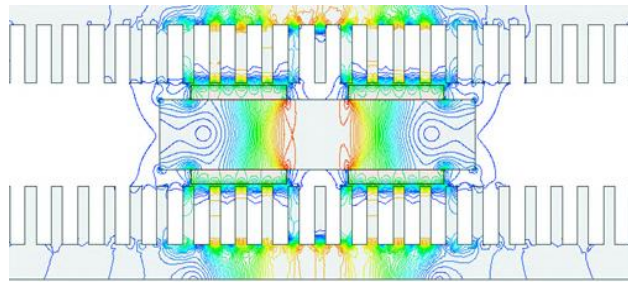


Fig.8. the flux lines in the motor

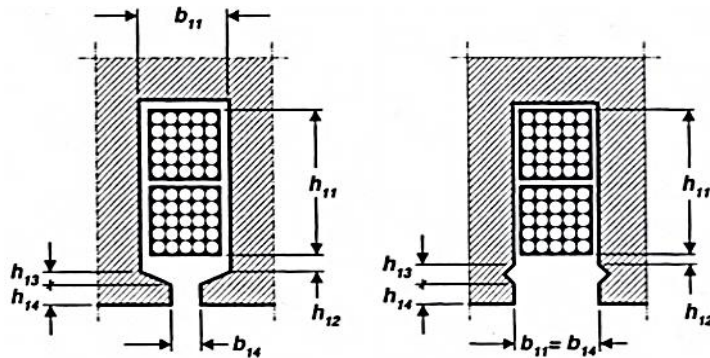


Fig.9. Armature slots: (a) semi-open, (b) open

Figure 10 illustrates a comparison between the detent force obtained using the semi-closed and open slots.

Results are obtained at a rotor speed of 10mm/s. As shown here, use of the semi-closed slots can reduce the detent force significantly, due to the decrease of cogging force. Figure 11 shows a comparison between the air gap flux density for semi-closed slot and open slot motor. The average flux density is observed to be more for the semi-closed slots, which supports increase of generated thrust of motor.

So the semi-closed slot motor is considered for optimization purposes. Figure 12 shows a comparison between the detent forces when the rotor thickness is changed ( $h_r$ ). As evident from Fig.13, the detent force is directly proportional with the thickness of rotor i.e. the

detent force increases with rotor thickness. Figure 13 shows the effect of variable thickness of PM ( $h_m$ ) on the detent force. The detent force is also directly proportional with PM thickness. By changing the width of PM, period of waveform of the detent force can be changed as shown in Fig. 14. The length of air gap also has impact on the detent force. Figure 15 shows the detent force in different air gaps. Increase in air gap reduces the detent force.

Another important parameter in reduction of the detent force is the arc on the PM surface which can be expressed in terms of pole offset as shown in Fig. 16. This has very significant effect on reducing the detent force. Figure 17 shows the detent force with variable pole offset. The higher the value of pole offset, the lesser is the detent force.

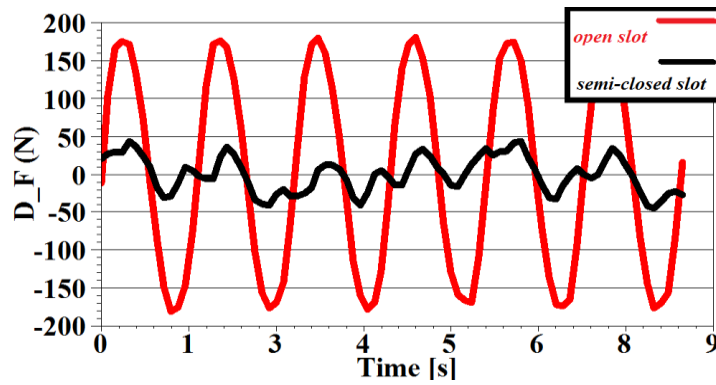


Fig. 10. Comparison between the detent force using the semi-closed slot and open slot motor

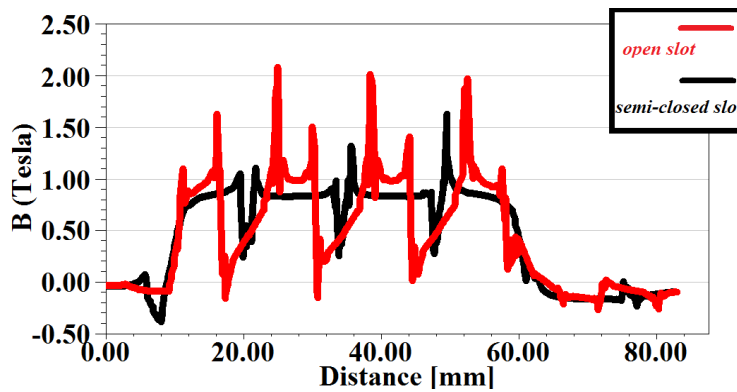


Fig. 11. Comparison between the air gap flux density using semi-closed slots and open slots

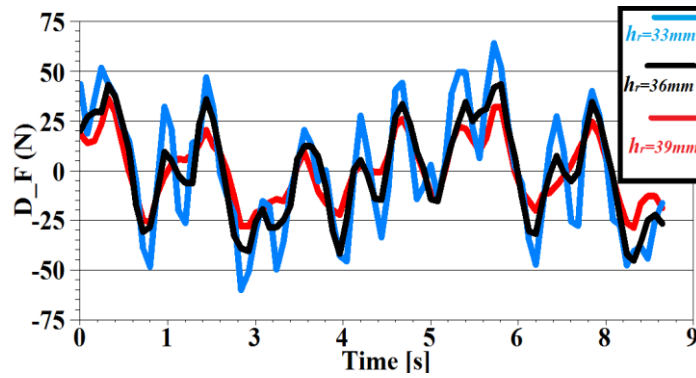


Fig. 12. Comparison between the detent forces when the rotor thickness is changed

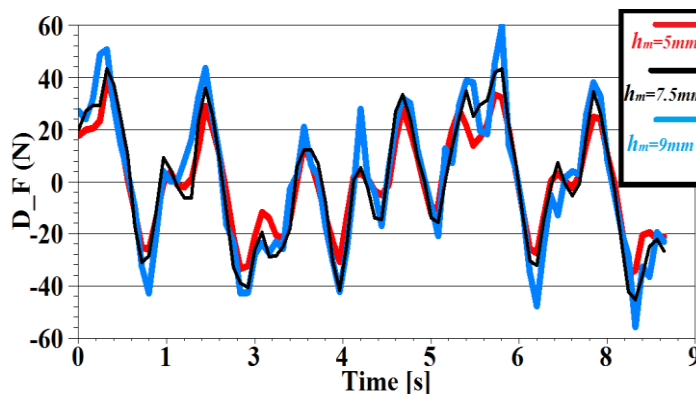


Fig. 13. Effect of change in PM thickness on the detent force

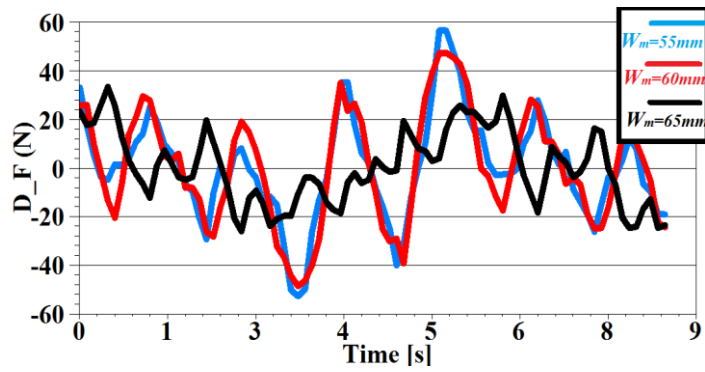


Fig. 14. Effect of change of width of PM on the detent force

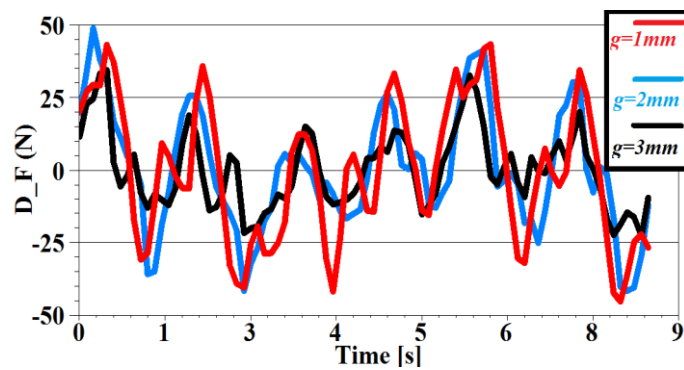


Fig. 15. Comparison between the detent forces when the air gap length is changed

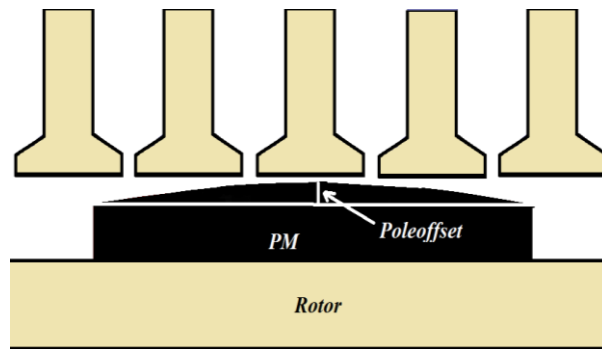


Fig. 16. Consideration of an offset for PM surface

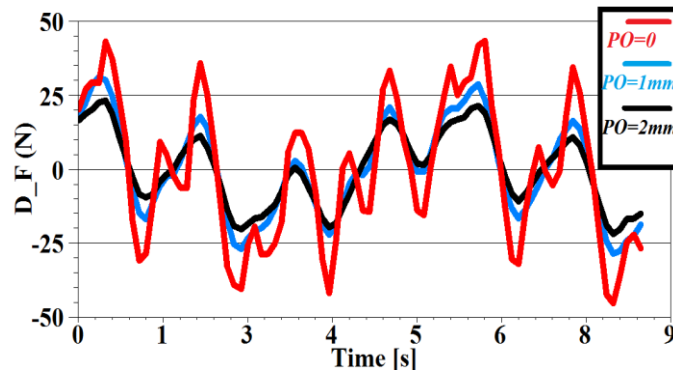


Fig. 17. The change in detent force with variable pole offset

#### 4.2. Optimization using genetic algorithm

In this paper, using genetic algorithm, optimization of the design of a motor structure to achieve the minimum detent force is studied. So, the objective function in this optimization problem is the value of the detent force.

As shown previously in this study, changes in the geometric parameters influence the detent force. Changing a parameter also changes the magnetic flux density in the air gap. In fact, we aim to achieve the minimum detent force without changing the magnetic flux density in the air gap. Therefore, problem optimization is accompanied by a constraint, i.e. unchanged magnetic flux density in the air gap. The objective function and problem constraint can be thus expressed as

$$OF = 1 + (\max|detent\ force| - |Detent\ Force_{min}|) \tag{12}$$

$$Con = 1 + (B_{avg} - B_{avgN}) \tag{13}$$

In Eq. (12) OF is the objective function where  $\max|detent\ force|$  is instantaneous maximum value of the detent force and  $|detent\ Force_{min}|$  is the minimum value of the detent force. In this equation  $OF=1$  is the goal to reach. Equation (13) shows the problem constraint where  $B_{avg}$  is average value of the magnetic flux density calculated in the air gap and  $B_{avgN}$  is nominal average value of the air gap magnetic flux density that is calculated using the geometric parameters in the Table 1.

In this Equation, the goal is  $Con=1$ .

In this optimization, three parameters are considered as design variables; the thickness of PM ( $h_m$ ), the width of PM ( $\omega_m$ ) and the pole offset (PO). Figure 18 shows the results of the iteration by the genetic algorithm. It is

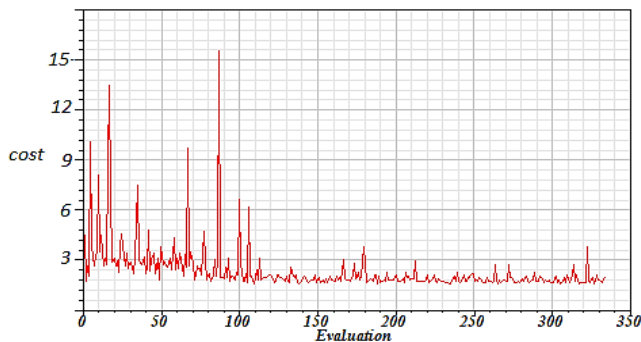


Fig. 18. Results of the iteration by Genetic Algorithm

observed that after some iteration, in spite of several mutations in the calculation, the results are converged finally to a certain value. The optimal parameters are listed in Table 2 which is related to the iteration 326.

Table 2. The optimal parameters which is related to the iteration 326

Symbol	Parameter Value
$h_m$	3.0163mm
$\omega_m$	51.4776mm
PO	3.571mm

Figure 19 shows the detent force obtained by the optimal parameters. Figure 20 illustrates a comparison of the detent force in the motor before and after the optimization.

Figure 21 shows a comparison of the magnetic flux density in the air gap before and after optimization. The results suggest that despite the reduction in the detent force, there is little difference in the air gap flux density of the two designs.

#### 5. Conclusions

The flux density distribution in the air gap was calculated by an analytic solution of Laplace and Poisson equations. This flux density distribution was expressed in terms of the motor geometric parameters, such as the width of the PM, the thickness of the PM, length of the rotor, thickness of the rotor and slot width. The detent force was computed by integrating the Maxwell stress tensor. Using the FEM, influence of the geometric parameters on the double-sided PMLSM was studied. Use of the semi-closed slots significantly reduces the detent force. Increase in the PM thickness also causes a reduction in the detent force. Increase in the PM width changed the period of the waveform of the

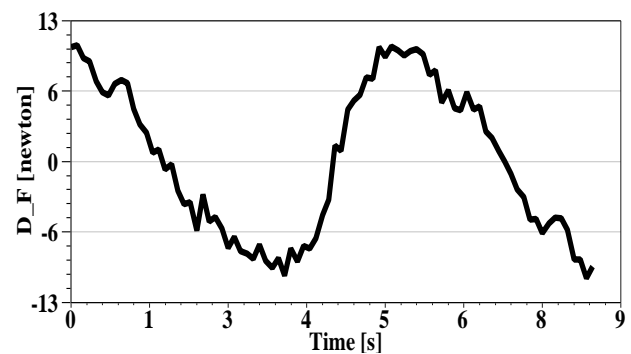


Fig. 19. The detent force obtained by the optimal parameters

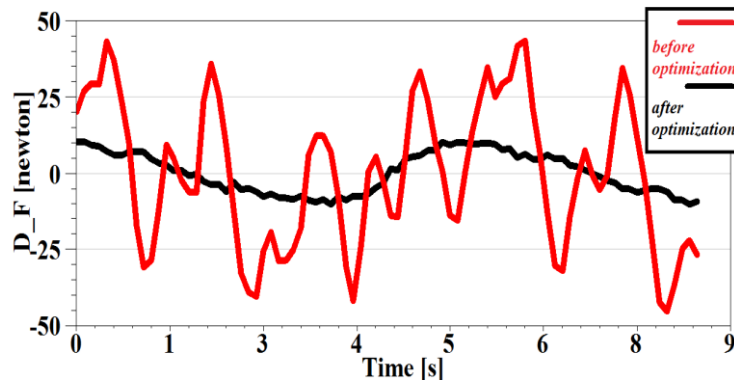


Fig. 20. Comparison of the detent force before and after the optimization

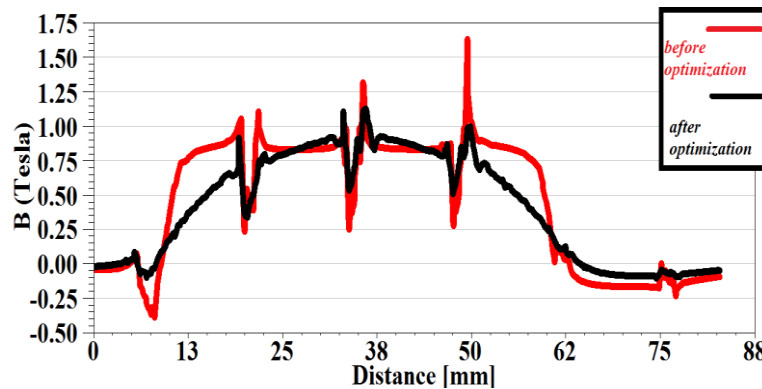


Fig. 21. Comparison of the magnetic flux density in the air gap before and after the optimization

detent force. Also, the pole offset of the PM improved the detent force. The optimized design was obtained using the genetic algorithm, considering the detent force as the objective function and unchanged flux density in the air gap as a constraint; and three major geometric parameters (PM thickness, PM width and PM pole offset) as design variables. Results indicate a reduction in the detent force and there is little difference in the average air gap magnetic flux density before and after the optimization.

## References

- [1] Kwon Y.S., Kim W.j., Detent-Force Minimization of Double-Sided Interior Permanent-Magnet Flat Linear Brushless Motor, *IEEE Transactions on Magnetics* (2016) 52: 8201609-8201609.
- [2] Gieras J. F., Piech Z. J., Tomczuk B. Z., *Topologies and Selection in Linear Synchronous Motors*, 2nd edition (2012) 1–22.
- [3] Ma M., Zhang J., Yu J., Zhang H., Jin Y., Analytical Methods for Minimizing Detent Force in Long-Stator PM Linear Motor Including Longitudinal End Effects, *IEEE Transactions on Magnetics*(2015) 51: 8204104- 8204104.
- [4] Wei Qian, T. A. Nondhal, Mutual torque ripple suppression of surface-mounted permanent magnet synchronous motor, *International Conference on Electrical Machines and Systems* (2005) 1: 315 – 320.
- [5] Youn S. W., Lee J. J., Yoon H. S., Koh C. S., A New Cogging-Free Permanent-Magnet Linear Motor, *IEEE Transactions on Magnetics* (2008) 44.: 1785–1790.
- [6] Jung I.S., Hur J., Hyun D. S., Performance Analysis of Skewed PM Linear Synchronous Motor According to Various Design Parameters, *IEEE Transactions on Magnetics* (2001) 37:373653–3657.
- [7] Zhu Y. W., Koo D. H., Cho Y. H., Detent Force Minimization of Permanent Magnet Linear Synchronous Motor by Means of Two Different Methods, *IEEE Transactions on Magnetics* (2008) 44: 4345–4348.
- [8] Hwang C. C., Li P. L., Liu C. T., Optimal Design of Permanent Magnet Synchronous Motor with Low Cogging Force, *IEEE Transactions on Magnetics* (2012) 48:1039–1042.
- [9] Tavana T.N.R., Shoulaie A., Pole-Shape Optimization of Permanent Magnet

- Linear Synchronous Motor for Reduction of Thrust Ripple, Energy Conversion and Management (2011) 52:349–354.
- [10] Bianchi N., Bolognani S., Cappello A. D. F., Reduction of Cogging Force in PM Linear Motors by Pole-Shifting, Proceedings - Electric Power (2005) 152: 703–709.
- [11] Lim K. C., Woo J. K., Kang G. H., Hong J. P., Kim G.-T., Detent Force Minimization Techniques in Permanent Magnet Linear Synchronous Motors, IEEE Transactions on Magnetics (2002) 38:1157–1160.
- [12] Inoue M., Sato K., An Approach to a Suitable Stator Length for Minimizing the Detent Force of Permanent Magnet Linear Synchronous Motors, IEEE Transactions on Magnetics (2000) 36: 1890–1893.
- [13] Inoue M., Sato K., An Approach to a Suitable Stator Length for Minimizing the Detent Force of Permanent Magnet Linear Synchronous Motors, IEEE Transactions on Magnetics (2000) 36:1890–1893.
- [14] Mikail R., Iqbal H., Sozer Y., Islam M., Sebastian T., Torque Ripple Minimization of Switched Reluctance Machines through Current Profiling, IEEE Transactions Applications (2013) 49: 1258 – 1267
- [15] Zare M.R., Marzband M., Calculation of Cogging Force in Permanent Magnet Linear Motor Using Analytical and Finite Element Methods, Majlesi Journal of Electrical Engineering (2010) 4:42-47.
- [16] Zhu L., Jiang S. Z., Zhu Z. Q., Chan C. C., Analytical Methods for Minimizing Cogging Torque in Permanent-Magnet Machines, IEEE Transactions on Magnetics (2009) 45: 2023–2031.
- [17] Li A. L., Ma B. M., Chen C. Q., Detent Force Analysis in Permanent Magnet Linear Synchronous Motor Considering Longitudinal End Effects, in Proceedings of the 15th International Conference on Electrical Machines System, Sapporo, Japan (2012) 1–5.
- [18] Binns K. J., Lawrenson J., Analysis and Computation of Electric and Magnetic Field Problems, Pergamon Press (1973) 95.
- [19] Jacek F. Gieras, Mitchell W., Permanent Magnet Motor Technology - Design and Applications, Marcel Dekker Incorporated (1973) 88.